



## Corrosion behaviour of WC-10% AISI 304 cemented carbides

A.B. Oliveira<sup>a</sup>, A.C. Bastos<sup>a,\*</sup>, C.M. Fernandes<sup>a,b</sup>, C.M.S. Pinho<sup>a</sup>, A.M.R. Senos<sup>a</sup>, E. Soares<sup>c</sup>, J. Sacramento<sup>c,d</sup>, M.L. Zheludkevich<sup>a,e</sup>, M.G.S. Ferreira<sup>a</sup>

<sup>a</sup> DEMaC—Department of Materials and Ceramic Engineering and CICECO, Aveiro Institute of Materials, University of Aveiro, 3810-193 Aveiro, Portugal

<sup>b</sup> ISEC, Mechanical Department, Engineering Institute of Coimbra, Rua Pedro Nunes, 3030-199 Coimbra, Portugal

<sup>c</sup> DURIT—Metalurgia Portuguesa do Tungsténio Lda, 3854-909 Albergaria-a-Velha, Portugal

<sup>d</sup> ESTGA—Águeda School of Technology and Management, University of Aveiro, 3754-909 Águeda, Portugal

<sup>e</sup> MagIC, Institute of Materials Research, Helmholtz-Zentrum Geesthacht, Max-Planck Str. 1, 21502 Geesthacht, Germany

### ARTICLE INFO

#### Article history:

Received 17 March 2015

Received in revised form 1 August 2015

Accepted 3 August 2015

Available online 4 August 2015

### ABSTRACT

The corrosion behavior of tungsten carbide hard metal composites with AISI 304L stainless steel as binder matrix and a WC-Co composite with similar grain size and binder content was investigated using electrochemical techniques (open circuit potential monitoring, current-potential curves, electrochemical impedance spectroscopy, scanning vibrating electrode technique) and scanning electron microscopy.

© 2015 Elsevier Ltd. All rights reserved.

#### Keywords:

A. Metal matrix composites

B. EIS

B. SEM

## 1. Introduction

Tungsten carbide hard metal composites are materials with a wide range of applications, being wear resistant parts for industrial applications and mining tools a particular niche of great importance [1]. The classical material consists of tungsten carbide (WC) hard particles in a ductile binder phase of cobalt (Co) [2]. The corrosion resistance of WC-Co composites can be unsatisfactory in certain areas such as the chemical and the oil and gas exploration industries [3]. WC-Co typically fails by corrosion of the less resistant phase, which is defined by the environment: in acidic solutions Co readily dissolves while WC is passive, the opposite occurring in alkaline media [4–8]. While the total or partial replacement of Co by Ni is already done industrially, the use of Ni/Fe binders is being investigated for a long time in order to improve the corrosion resistance of the binder and reduce the costs associated with the short supply and high market quotation of cobalt powder [9]. WC-Ni-Fe based hard metals are reported to present much better corrosion resistance in acidic media compared to WC-Co [10]. The same was observed for WC-VC-Co [11].

The improvement of corrosion resistance does not exclusively depend on the binder composition; the WC grain size may also

play an important role. The available information, however, is contradictory: according to some authors, the smaller the grain size the higher the corrosion resistance [4,12], while other authors did not find any grain size effect on the corrosion rate of WC-Co [13–15]. The erosion-corrosion resistance of micro-crystalline and near-nanocrystalline cermet coatings applied by high velocity oxy-fuel (HVOF) thermal spray was studied [16] and results showed approximately one third lower erosion-corrosion rate of the near-nanocrystalline coatings compared to the microcrystalline ones. Preliminary results showed that the erosion-corrosion mechanism in the coatings was dominated by pure erosion in the microcrystalline coating and corrosion enhanced erosion in the near-nanocrystalline coating. Fedrizzi et al. also studied the tribocorrosion of several cermet coatings applied by HVOF in chloride media [17] and observed that when chromium was alloyed in the metal matrix of WC based systems lower tribocorrosion rates were measured. The corrosion of WC-Co hard metals has also been studied in other environments, such as high temperature oxidation (at 500 °C [18] and up to 850 °C [19]) or exposure to sulphate reducing bacteria in oil-in-water emulsions to simulate metalworking fluids used for corrosion inhibition, cooling and lubrication [20].

Work is still ongoing in search of new binders for this type of material. In a previous study [21] conventional powder metallurgy routes were used to prepare compositions using AISI 304L stainless steel (SS) as binder for WC particles. A compromise was obtained between hardness and fracture toughness with values higher than

\* Corresponding author.

E-mail address: [acbastos@ua.pt](mailto:acbastos@ua.pt) (A.C. Bastos).

**Table 1**  
Composition of the studied composites.

	Composition (wt.%)			
	WC	Co	304 LSS	C
WC-Co	90	10	—	—
WC-SS	90	—	10	—
WC-SS-C	89.7	—	10	0.3

the traditional WC-Co system. The Young's modulus was similar to WC-Co but the transverse rupture strength was lower. This was overcome by addition of a small amount of carbon (0.3 wt.%) which reduced significantly the  $\eta$ -phase, increasing the strength of WC grain boundaries and the average transverse rupture strength.

In this work the corrosion behavior of those compositions and a WC-Co composite with similar grain size and binder amount is compared in NaCl solution using electrochemical methods (open circuit potential monitoring, anodic and cathodic polarization curves, polarization resistance method, electrochemical impedance spectroscopy, scanning vibrating electrode technique) and scanning electron microscopy (SEM) coupled with energy dispersive X-ray spectroscopy (EDS).

## 2. Experimental

### 2.1. Materials processing

Tungsten carbide (H.C. Starck, Germany) and AISI 304L stainless steel powders (Sandvik, Sweden) with a mean particle size of 9.1  $\mu\text{m}$  and 10  $\mu\text{m}$ , respectively, were used as raw materials. The composition of the AISI 304L stainless steel (SS) was (wt.%): Fe, 70; Cr, 18; Ni, 10; Mn, 2; C < 0.03, as given by the producer. Taking into account the controlling effect of C on the formation of  $\eta$ -phase in the WC-SS system [22] and based on the WC-Fe-Ni phase diagram [23], carbon lump powder (Panreac 1221, Spain) was added to adjust the carbon content.

The proportionate powders were blended in a planetary ball mill with WC-Co balls during 12 + 2 h at 150 rpm using 2-propanol as milling medium (the mixing in the last 2 h included 1.5 wt.% of paraffin wax). The powders were dried for 12 h at 60 °C and sieved (63  $\mu\text{m}$  mesh). Then, the powders were uniaxially pressed at 190 MPa giving samples of cylindrical shape with 10 mm diameter and 3 mm thickness, further submitted to cold isostatic pressing (CIP) at 330 MPa during 15 min. Sintering of the compacted samples was carried out in vacuum atmosphere (20 Pa) at a maximum temperature of 1450 °C during 120 min. The sintering conditions were optimised in a previous work [24].

Compositions of WC - 10 wt.% SS and WC - 10 wt.% SS - 0.3 wt.% C were prepared, hereafter referred as WC-SS and WC-SS-C, respectively. The starting volume of SS was 18% with respect to the volume of the total mixture. For comparison, a WC-Co sample with similar amount of binder (Co, 10 wt.%, 16 vol.%) and prepared with the same WC powder type was provided by a local hard metal manufacturer. Table 1 summarizes the composites studied in this work.

### 2.2. Microstructural characterization

Microstructural characterization was performed using a Hitachi SU-70 Schottky emission scanning electron microscope (15 kV accelerating voltage, 15 mm working distance) and a Quantax 400 energy dispersive X-ray spectrometer from Bruker. Rietveld analyses of X-ray diffraction (Philips X'Pert diffractometer with a step size of 0.02° ( $2\theta$ ) and a counting time of 3 s per step) provided qualitative and quantitative structural information.

The area of the different phases on polished surfaces of the composites was determined by digital analysis (pixel counting after

picture binarization) using Image J software [25]. For each system a minimum of four SEM pictures was employed, each picture with 440  $\mu\text{m}^2$  and having been randomly acquired on the sample surface.

### 2.3. Electrochemical measurements

The specimens were mounted in resin using a Struers LaboPress-3 metallurgical mounting press, followed by grinding in 220, 500, and 1200-grit silicon carbide sandpaper and polishing using diamond pastes with sizes of 6, 1 and 0.25  $\mu\text{m}$ . The mounts were washed in ethanol and distilled water. The samples were electrically connected from the back.

Current-potential curves and electrochemical impedance spectroscopy (EIS) were performed with a PGSTAT302N Potentiostat/Galvanostat (Autolab Methrom) in a three electrode arrangement with the sample as working electrode, a large coiled platinum wire as the counter electrode and a Saturated calomel electrode (SCE) with a Luggin-Haber capillary as reference. The tip of the capillary was placed 2 mm away from the working electrode surface in order to reduce the IR drop. The 2 mm corresponds to twice the tip diameter to avoid shielding the current flux. All experiments were performed inside a Faraday cage.

The open circuit potential (OCP) was monitored against SCE. Anodic and cathodic current-potential curves were measured after 1 h of sample immersion with a scan rate of 1  $\text{mV s}^{-1}$  in the positive (anodic branch) or the negative (cathodic branch) directions starting near OCP. Measurements of the polarization resistance were performed with new samples after 1 h of immersion, polarising from  $-10 \text{ mV}$  to  $+10 \text{ mV}$  (vs OCP) with a scan rate of 1  $\text{mV s}^{-1}$ .

EIS spectra were obtained at open circuit potential, with a sinusoidal signal of 10 mV rms amplitude, in the 100 kHz–1 mHz frequency range with 7 points per decade logarithmically distributed. Numerical fitting of the spectra was made using the ZView software (Scribner Associates, USA).

The spatial distribution of corrosion was assessed by the scanning vibrating electrode technique (SVET) with equipment manufactured by Applicable Electronics Inc. (USA) and software developed by Science Wares Inc. (USA). The vibrating microelectrode was a 250  $\mu\text{m}$  diameter platinum-iridium wire thinned to a tip of  $\sim 3 \mu\text{m}$  and covered, except for the tip, by insulating polyethylene C® polymer. A 20  $\mu\text{m}$  platinum black deposit was grown on the tip to increase sensitivity. Each scan comprised 50 × 50 points and was measured at an average distance of 200  $\mu\text{m}$  from the surface with the electrode vibrating at 89 Hz and 10  $\mu\text{m}$  amplitude.

The sample area in the various electrochemical experiments varied between 0.3 and 1  $\text{cm}^2$ . In all cases the testing solution was quiescent naturally aerated aqueous 0.05 M NaCl. This relatively low concentration was chosen to facilitate SVET measurements and to slow down the corrosion for the detection of transient features of the process.

## 3. Results

### 3.1. Structural and microstructural characterization

XRD analysis of WC-SS and WC-SS-C is shown in Fig. 1. In both composites WC is the major phase with a small signal from  $\gamma$ -Fe (austenite).  $\eta$ -phase was detected in WC-SS. It may exist in WC-SS-C but in less than 2 wt.% since it was not detected by XRD. The composition of this phase has been reported to be  $(\text{Fe}_{2.3}\text{Ni}_{0.3})(\text{Cr}_{0.6}\text{W}_{2.8})\text{C}$  [22].

The morphology of the composites was investigated by SEM/EDS on polished surfaces (Fig. 2). The WC phase corresponds to the lighter grey color, whilst the austenite binder phase corresponds to

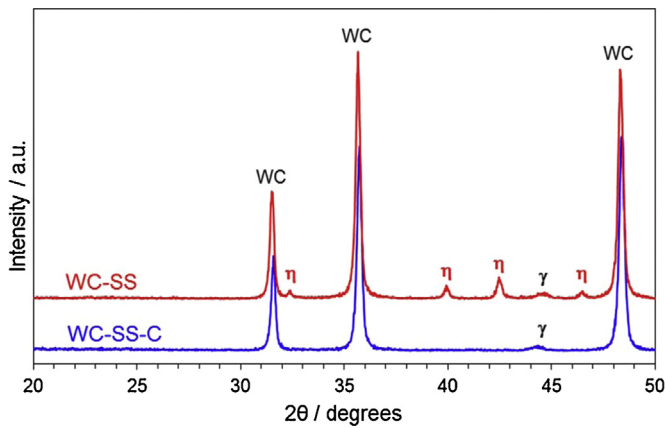


**Fig. 1.** Diffractograms of WC-SS and WC-SS-C sintered samples, with peaks from tungsten carbide (WC), eta-phase ( $\eta$ ) and austenite ( $\gamma$ ).

**Table 2**  
Percent area of the different phases in each composite.

	Area of the phase (%)			
	WC	Co rich phase	Fe rich phase	$\eta$
WC-Co	84	16	–	–
WC-SS	77	–	11	12
WC-SS-C	82	–	18	–

the darkest areas surrounding the WC grains. The carbon-deficient  $\eta$ -phase appears with an intermediate grey color in a sort of “islands”, frequently in WC-SS (Fig. 2a) and rarely in WC-SS-C (Fig. 2b). The formation of  $\eta$ -phase is thermodynamically favored in WC-SS when carbon is present in stoichiometric proportion with respect to WC [22,23]. An excess of carbon prevents its formation.

The surface of the WC-Co composite used in this work is shown in Fig. 3 for comparison. The WC particles size and distribution are similar to that of WC-SS-C. Table 2 presents the area fraction of the

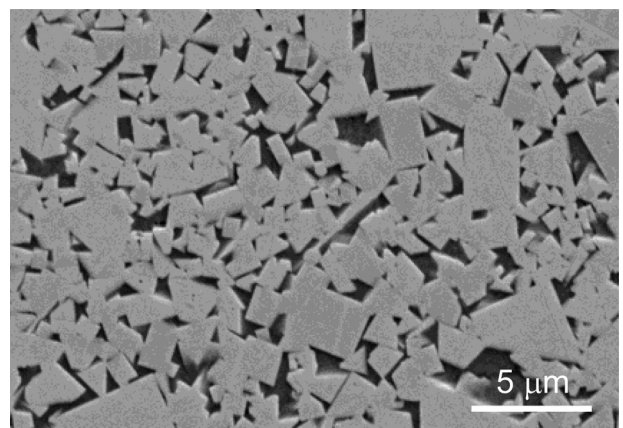


**Fig. 3.** SEM image of the surface of WC-Co.

phases of each composite determined by digital analysis of SEM images. The areas depend on the initial constituent amounts but also on the reactions occurring during sintering: formation of mixed carbide phases, such as  $\eta$ -phase, volatilization and dissolution of tungsten and/or carbon in the metallic liquid phase. Therefore, the areas can be very different for identical initial binder contents, as in the case of WC-SS and WC-SS-C, due to the formation of a significant amount of  $\eta$ -phase in the former. The area of SS in WC-SS-C is similar to the area of Co in WC-Co.

During the processing steps, caution was paid to avoid porosity because it has a strong influence on the mechanical properties, especially on hardness and transverse rupture strength. Residual porosity, particularly large pores, is enough to cause catastrophic failure [26]. In both composites the porosity level was less than 0.3%.

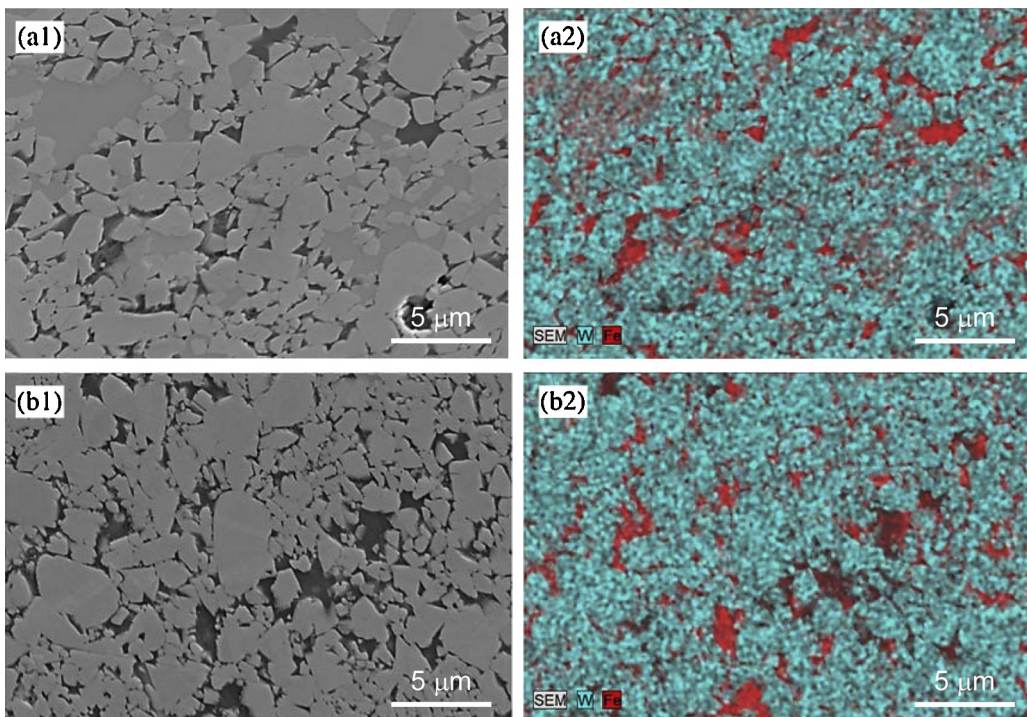


**Fig. 2.** SEM images and corresponding EDS X-ray elemental maps of (a) WC-SS and (b) WC-SS-C.

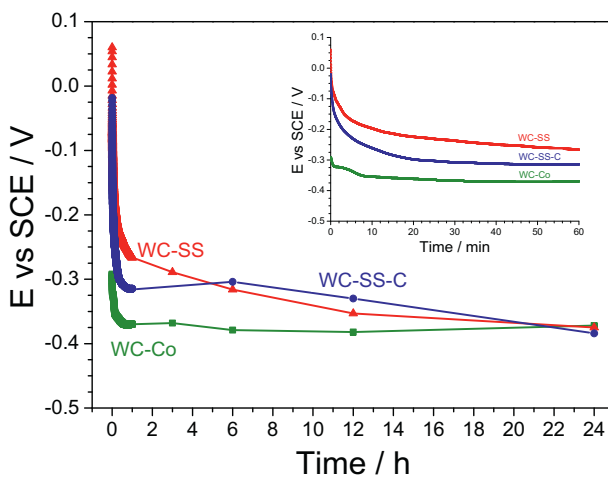


**Fig. 4.** OCP measurements of WC-Co, WC-SS and WC-SS-C.

### 3.2. Electrochemical response in corrosive medium

#### 3.2.1. Open circuit potential monitoring

Fig. 4 shows the OCP of the samples during the first day of immersion in 0.05 M NaCl. A marked decrease in potential occurred in all samples in the first minutes of immersion. WC-Co was the first to stabilise, after  $\sim 30$  min, at values that remained fairly constant until the end of the test ( $-0.365$  V vs SCE). The potential of the new composites was more positive but slowly decreased until attaining values very close to WC-Co by the end of the testing period.

#### 3.2.2. Current-potential curves

Potentiodynamic polarization curves measured after one hour of immersion in 0.05 M NaCl are presented in Fig. 5. The cathodic branches, Fig. 5(a), depict well defined limiting plateaus for the oxygen reduction, ranging between  $2.5$  and  $5.5 \times 10^{-5} \text{ A cm}^{-2}$ . A Tafel region about 0.25 V wide was observed for WC-SS, slightly smaller for WC-SS-C and absent in WC-Co. This suggests activation control of the  $\text{O}_2$  reduction close to OCP for the composites with AISI 304 binder while for WC-Co the reaction is rapid enough for the control to be readily diffusional. Hydrogen evolution dominates the WC-Co curve for potentials more negative than  $-1$  V<sub>SCE</sub> and  $-1.1$  V<sub>SCE</sub> for the new composites. In the anodic polarization curves (Fig. 5b) no passive regions were observed near the corrosion potential.

To later compare with the  $R_{\text{ct}}$  parameter obtained by EIS, the polarization resistance,  $R_p$ , was measured in dedicated experiments whose results are presented as inset of Fig. 5b.  $R_p$  values of  $11,902$ ,  $3435$  and  $2407 \Omega \text{cm}^2$  were obtained respectively for WC-SS, WC-SS-C and WC-Co.

#### 3.2.3. Electrochemical impedance spectroscopy

Fig. 6 presents EIS spectra in Bode and Nyquist format recorded at selected times during the first 24 h of immersion. WC-Co showed one well defined time constant response with a small decrease of impedance from the first to the third hour of immersion. Then the values remained practically constant, in line to what has been reported before [6]. With time, a new relaxation process appeared at higher frequencies and another one at lower frequencies. The impedance of the new composites was significantly higher than that of WC-Co, particularly for WC-SS. It was characterised by a two time constant response and a decrease of the impedance modulus with time. The low frequency values of impedance are of the same order of magnitude of  $R_p$  obtained by the polarization resistance method and follow identical order.

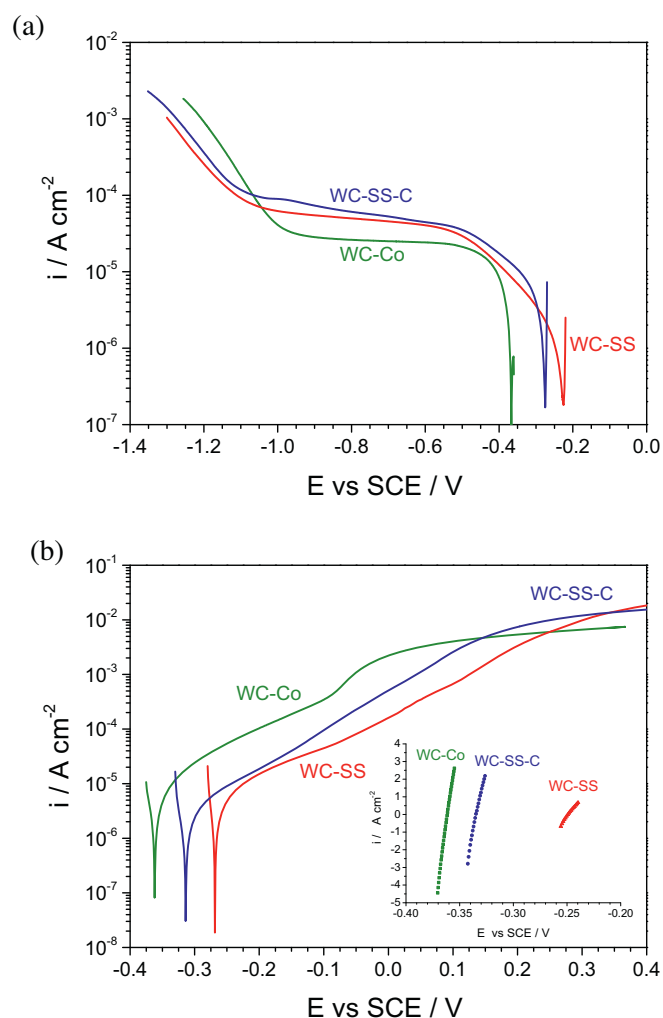


**Fig. 5.** Cathodic (a) and anodic (b) current-potential curves of WC-Co, WC-SS and WC-SS-C. The inset shows the polarization resistance curves of the three composites.

#### 3.2.4. Scanning vibrating electrode technique

The previous techniques give the global response of the corroding surface. Localized information was provided by the SVET. Maps obtained after 1 and 20 h of immersion are presented in Fig. 7. In WC-Co two intense pits appeared in the beginning of immersion, one being still very active after 20 h. Two pits were also observed in WC-SS at the beginning of immersion. By the end of the test, one pit was active together with other four of smaller intensity. Also two pits were active in WC-SS-C from the beginning until the end of immersion. In the three composites the remaining area showed cathodic activity. This indicates that the surface of all samples was electrochemically active. The optical pictures acquired with the SVET maps revealed more attack than that measured by SVET. This is well evidenced in the map and picture of WC-SS measured after 1 h of immersion. Some pits have been formed and became inactive before the map was acquired.

### 3.3. Scanning electron microscopy

Microscopic inspection was very helpful to understand the degree and morphology of attack. Fig. 8(a) shows the surface of WC-Co after 20 h of immersion. A region that gave strong anodic signal in the SVET map is clearly visible after a slight abrasion – Fig. 8(b) – revealing significant attack of the binder. Fig. 8(c) shows the border between the attacked area and the region that was

cathodic in the SVET maps. Clear distinction exists, with strong Co dissolution on the attacked side. Fig. 8(e) shows the corroded area in great detail. No signs of corrosion were found on the WC particles. Figs. 8(d) and (f) present the border after light abrasion and a detail of the corroded area, with loss of binder and WC particles.

Turning to WC-SS, Fig. 9(a) is the optical image of the SVET sample after testing (20 h immersion) and Fig. 9(b) is the SEM image of the same area after removing non adherent corrosion products. Fig. 9(c) shows the strongest anodic region, source of most of the corrosion products observed on the sample. No single deep hole exists, rather a few small pits, which are seen in more detail in Fig. 9(d). It was from these points that emanated the intense current detected by SVET. This same region was observed after abrading the surface and a wide attacked area was revealed beneath the original small pits – Fig. 9(e). This picture shows that corrosion took place by dissolution of the binder beneath the surface, undermining a large area which grew laterally with small thickness, not in depth. Fig. 9(f) shows the WC particles in the bottom of this area. No evidences of corrosion of WC were found. The  $\eta$ -phase also did not corrode, as it was found free of attack at all instances it was observed during the inspection of the surface after testing. Fig. 10 is a clear and representative example of it. Fig. 10 also reveals small pits distributed along the surface. They were too small, or too short lived, to be detected by SVET.

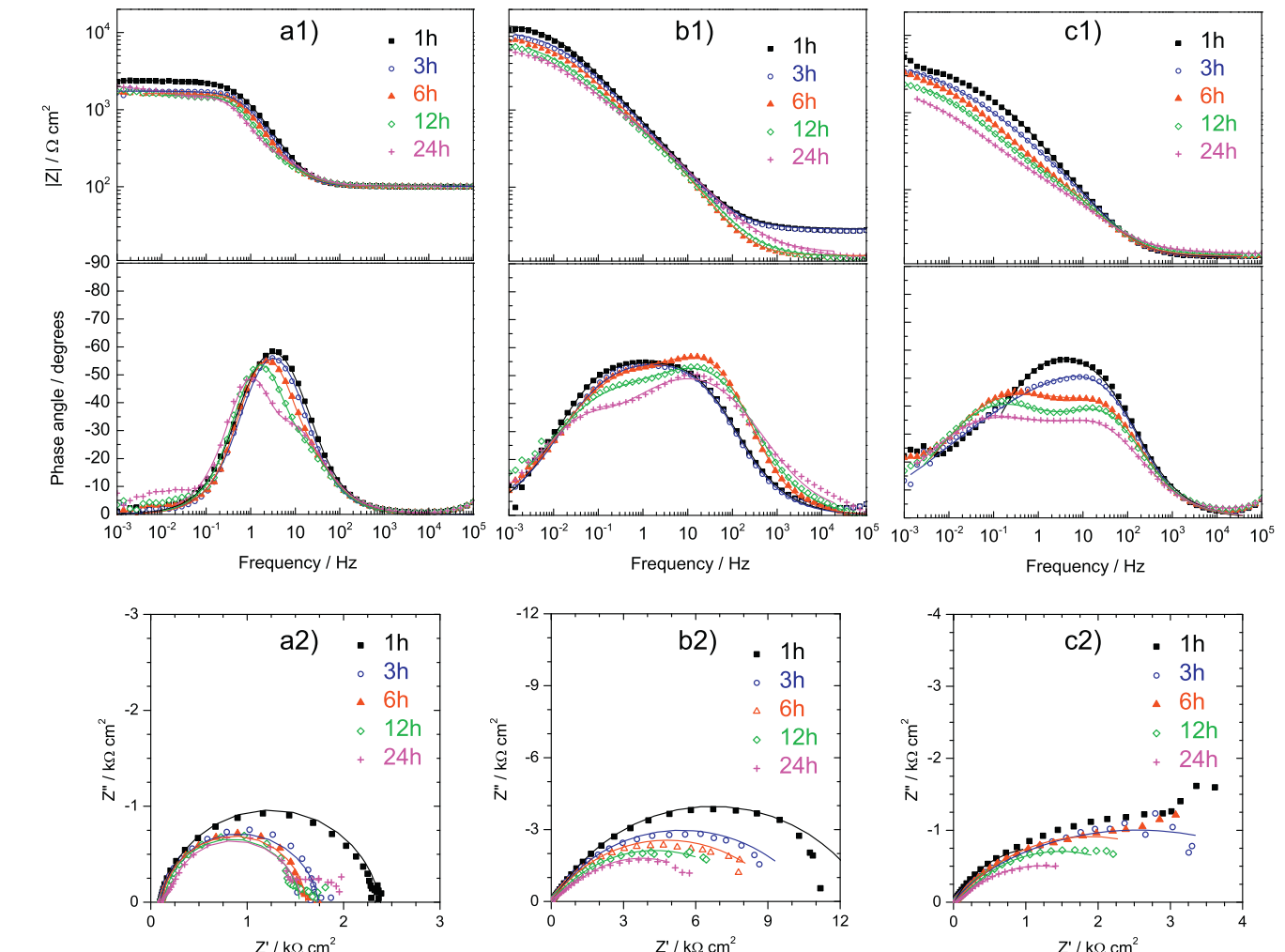
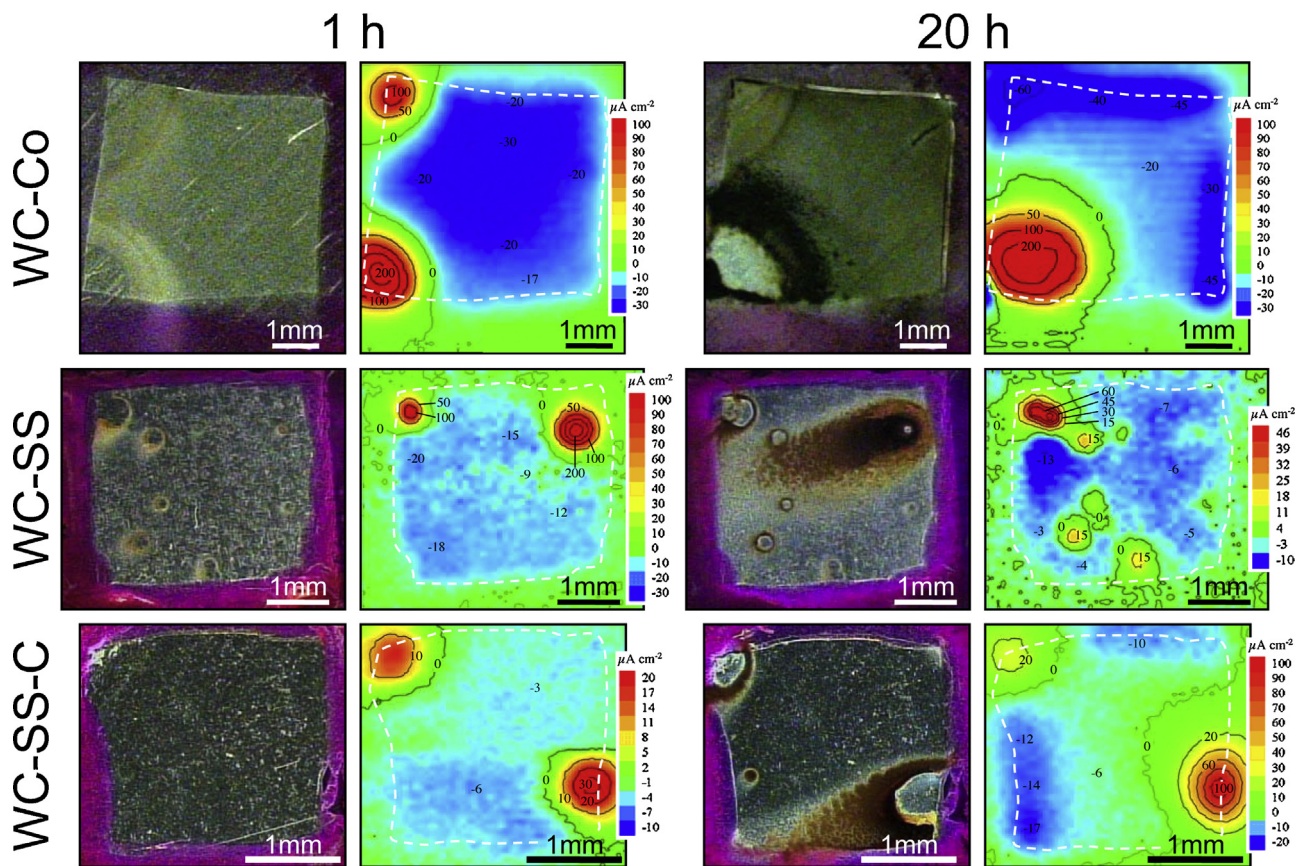


**Fig. 6.** Bode and Nyquist representations of the impedance spectra of (a) WC-Co, (b) WC-SS and (c) WC-SS-C during the first 24 h of immersion in 0.05 M NaCl. The experimental data is shown as points and the fitting results as lines.

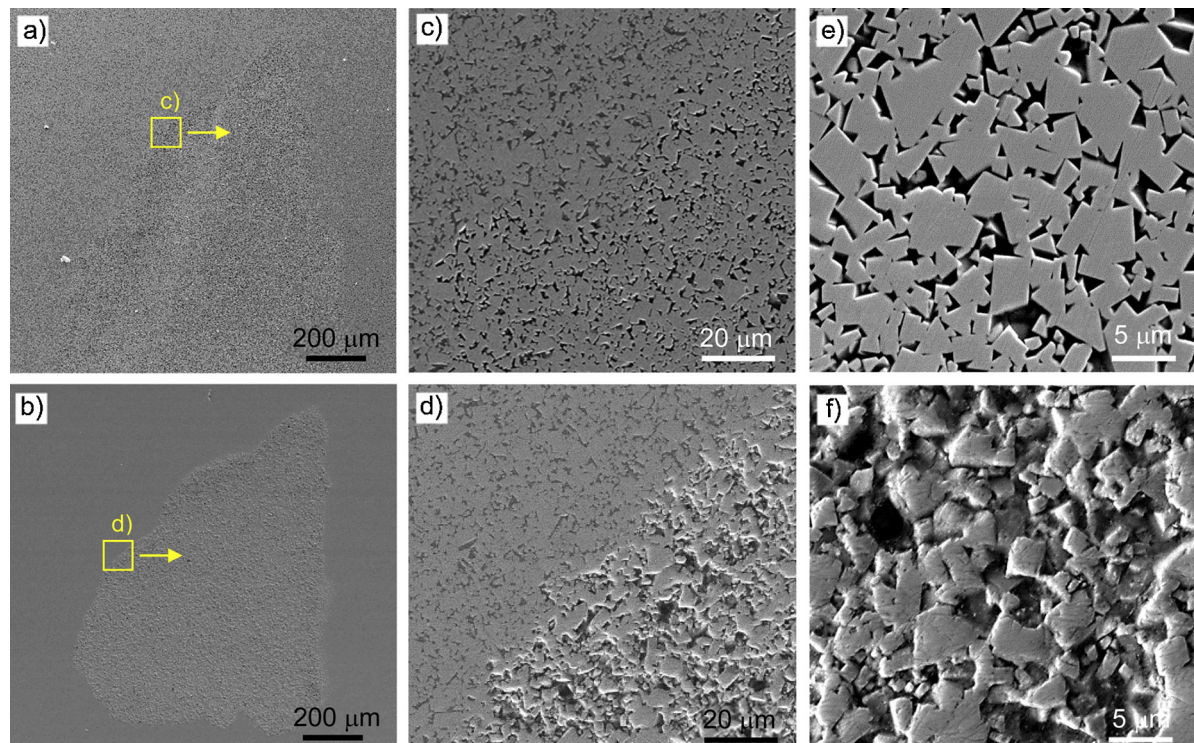
In WC-SS only the binder phase corroded and it occurred at 3 different rates: (i) uniform dissolution of the binder everywhere it was exposed, (ii) localised corrosion in small pits scattered through the surface and (iii) intense activity in a few pits with anodic undermining of the binder.

Fig. 11(a) shows WC-SS-C after 20 h of corrosion (end of SVET testing). The surface after removing the loose corrosion products is presented in Fig. 11(b). The most severely corroded areas were similar to what has been observed in Fig. 9 for WC-SS. Fig. 11(c) shows an area in the pit region with a layer of corrosion products above the surface with no clear signs of attack, except for a small uniform dissolution of the metallic binder. Fig. 11(d) displays the central region of the sample, where no pits were detected by SVET. Magnification and a slight abrasion revealed small corrosion spots distributed along the surface. Figs 11(e) and (f) are magnifications of, respectively, one area with practically no attack and another that suffered local binder dissolution.

A few conclusions can be drawn from the SEM observations of the composites: (i) no corrosion was found on WC particles, ii) the  $\eta$ -phase also did not reveal any signs of attack, (iii) the only corroding phase was the metallic binder (Co or  $\gamma$ -Fe rich phases); (iv) the three composites showed superficial and uniform dissolution in the exposed phase, (v) in just a few points intense corrosion took place with dissolution of the metallic binder beneath the sur-



**Fig. 7.** Optical images and SVET current density maps of WC-Co, WC-SS and WC-SS-C acquired after 1 h and 20 h of immersion. The white dashed line delimits the exposed surface.



**Fig. 8.** Microscopic characterization of the corrosion of WC-Co. (a) Corroded area after 20 h of immersion in 0.05 M NaCl; (b) the same area after a slight abrasion; (c) a detail of the border of the corroded and non corroded areas in (a); (d) a detail of the border of the corroded and non corroded areas in (b); (e) a magnification of the corroded area after 20 h of immersion; (f) magnification of the corroded area after slight abrasion.

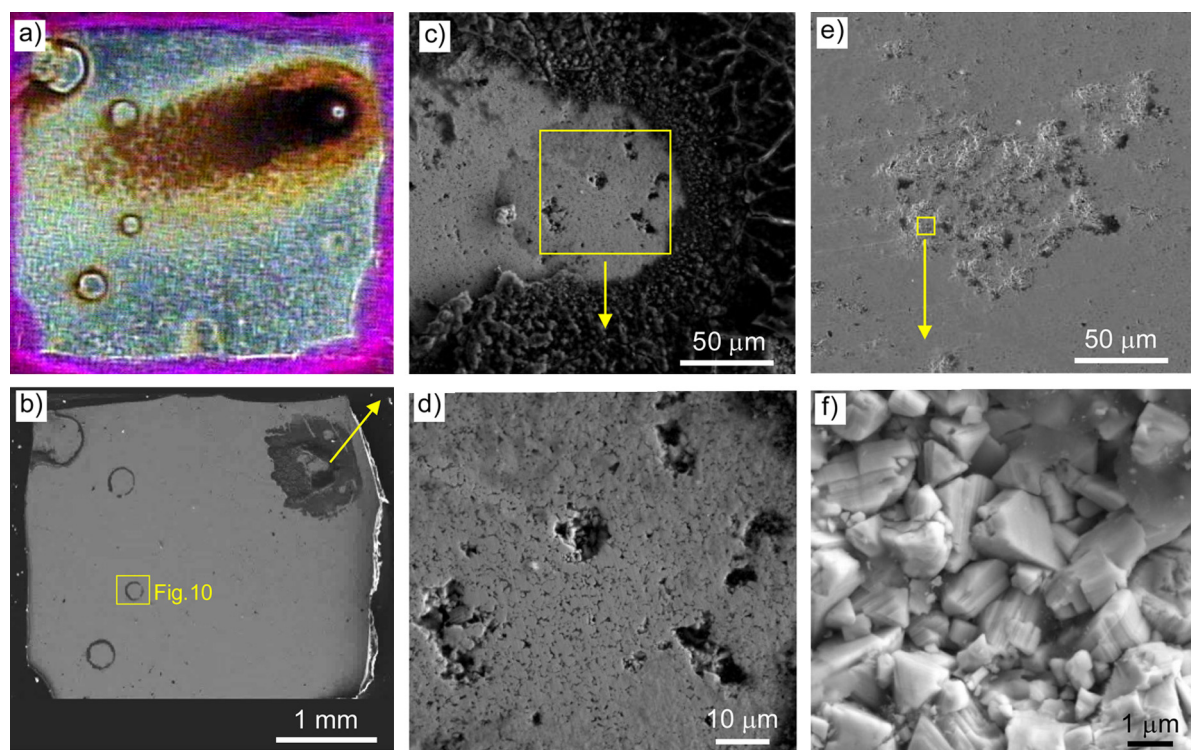


**Fig. 9.** Microscopic characterization of the corrosion of WC-SS. (a) Optical image of a sample after 20 h of immersion in 0.05 M NaCl; (b) SEM image of the same surface after removal of loose corrosion products; (c) a detail of the most corroded region of the sample; (d) a detail of (c); (e) the same area as (c) after abrasion, revealing a hollow corroded area beneath the surface; (f) magnification of the corroded area in (e).

face, (vi) in the samples containing 304L SS as binder, small pits developed scattered along the surface.

#### 4. Discussion

Based on the experimental results and considering the literature [6,7,15] it is possible to advance a possible mechanism for the degradation of these hard-metal composites. An important aspect is that no signs of passivity were found. The exposed metallic phase oxidizes since the beginning of the immersion with the reduction of dissolved O<sub>2</sub> occurring mainly at the WC phase. In some points the metal dissolves faster giving origin to small pits. In the new com-

posites the dissolution of some pits is so fast that continues beneath the surface undermining the material. The attacked area is larger than the one expected from the simple observation of the surface. Corrosion underneath the surface propagates more laterally than in depth. Metal oxidation is believed to be the main reaction in the undermined regions, since the reduction of O<sub>2</sub> is not likely to occur due to its limited access to such internal locations. Hydrolysis of the metal cations can acidify the internal solution creating conditions for an acceleration of corrosion of Co [8] and SS [27]. Another change in local pH takes place in the cathodic regions, coincident with the WC phase. The cathodic oxygen reduction increases the local pH promoting conditions for the dissolution of WC [7]. While

**Table 3**  
EIS fit parameters.

		R <sub>pit</sub> ( $\Omega \text{cm}^2$ )	C <sub>surf</sub> ( $10^{-5} \text{ Fcm}^{-2}$ )	C <sub>dl</sub> ( $10^{-5} \text{ Fcm}^{-2}$ )	R <sub>ct</sub> ( $\Omega \text{cm}^2$ )	$10^4 \chi^2$
WC-Co	1 h		8.95		2225 <sup>a</sup>	11
	3 h		10.9		1649 <sup>a</sup>	29
	6 h	132.7	8.39	6.92	1373	11
	12 h	163.2	9.00	13.2	1254	20
	24 h	317.0	9.29	22.5	1134	13
WC-SS	1 h	2672	4.60	4.62	11001	1.3
	3 h	1336	5.29	8.68	8654	1.7
	6 h	629	5.29	19.4	7970	1.8
	12 h	921	3.85	19.1	6779	2.7
	24 h	1879	2.27	85.1	4292	14
WC-SS-C	1 h		7.60		7447 <sup>a</sup>	85
	3 h	135.2	8.38	4.21	5404	3.1
	6 h	132.3	9.00	31.0	3456	4
	12 h	142.2	8.71	73.0	2649	5
	24 h	126.8	9.54	99.1	2073	2

<sup>a</sup> R<sub>surf</sub>.

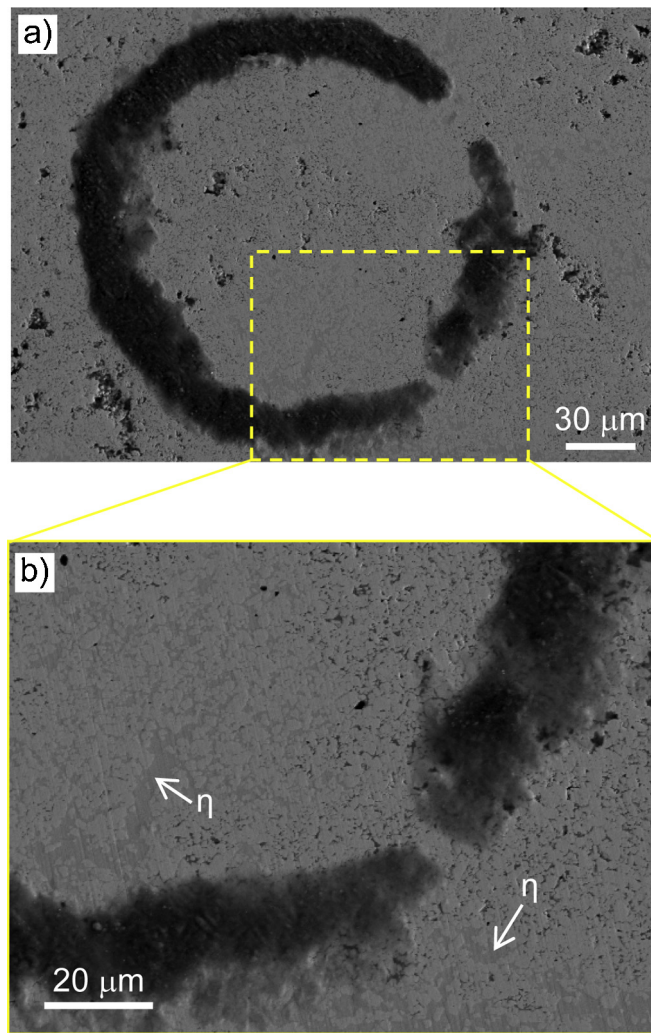


**Fig. 10.** Detail of corroded WC-SS highlighting small pits on the surface and the corrosion resistance of  $\eta$ -phase.

no signs of corrosion were observed on WC after 24 h of immersion, it may take place for longer exposure times.

The impedance response can be interpreted in the light of what has just been described. Fig. 12 is a sketch with the evolution of equivalent electric circuits that can mimic the measured impedance. At the beginning there is only one time constant response, addressed to the electrochemical processes at the surface, that is, the response of the double layer capacitance,  $C_{dl}$ , and of the charge transfer resistance,  $R_{ct}$ . It is possible to think in a separation of anodic and cathodic regions, represented by circuit a1, where the superscripts A and C stand for anodic and cathodic, respectively. Since the two RC are in parallel, the measured response can be described simply by circuit a2, a single parallel  $RC$  that incorporates all the small contributions distributed along the surface but dominated by the smallest  $R$  and the highest  $C$ . The surf subscript is a general designation intending to cover all possible contributions operating at the surface. For example, the surface capacitance includes the electrical double layer and the eventual influence of incipient surface films of corrosion products that may appear with time. Circuit a2 describes the impedance measured at the beginning of immersion. Then, in just a few hours, a second time constant appears. This seems to coincide with the onset of pits with undermining activity. As soon as the pits are deep enough, a new resistance appears (called here  $R_{pit}$  because it corresponds to the

resistance of solution inside the pits). Starting from this moment the  $R_{ct}$  and  $C_{dl}$  in the undermined regions are no longer in parallel with the remaining  $R$  and  $C$  elements at the surface (the degeneracy between them is broken by  $R_{pit}$ ). Circuit b1 gives a visual representation of the state of the surface and the correspondent equivalent electric circuit.  $R_{pit}$  is believed to be the same everywhere inside the pit. If the undermined area grows deep,  $R_{pit}$  may vary significantly and a new circuit with a transmission line has to be used to describe the impedance inside the pit. Since all  $R_{surf}$  and  $C_{surf}$  are in parallel and the same applies for  $R_{ct}$  and  $C_{dl}$  inside the pits, circuit b1 can be simplified to circuit b2, and further simplified to circuit b3 if  $R_{pit}$  is smaller than  $R_{surf}$ .

Circuits a2 and b3 were used to numerically fit the experimental spectra. In Fig. 6, points are experimental data and lines are fitting results. Constant phase elements (CPE) were used in place of capacitances due to dispersion of time constants resulting from surface heterogeneities and distributions of reactivity on the electrode surface [28]. The fitted CPE values were converted to capacitances using the equation from Brug et al. [29],

$$C = \sqrt[n]{Y_0} \left( \frac{1}{R_{series}} + \frac{1}{R_{parallel}} \right)^{\frac{n}{n-1}} \quad (1)$$

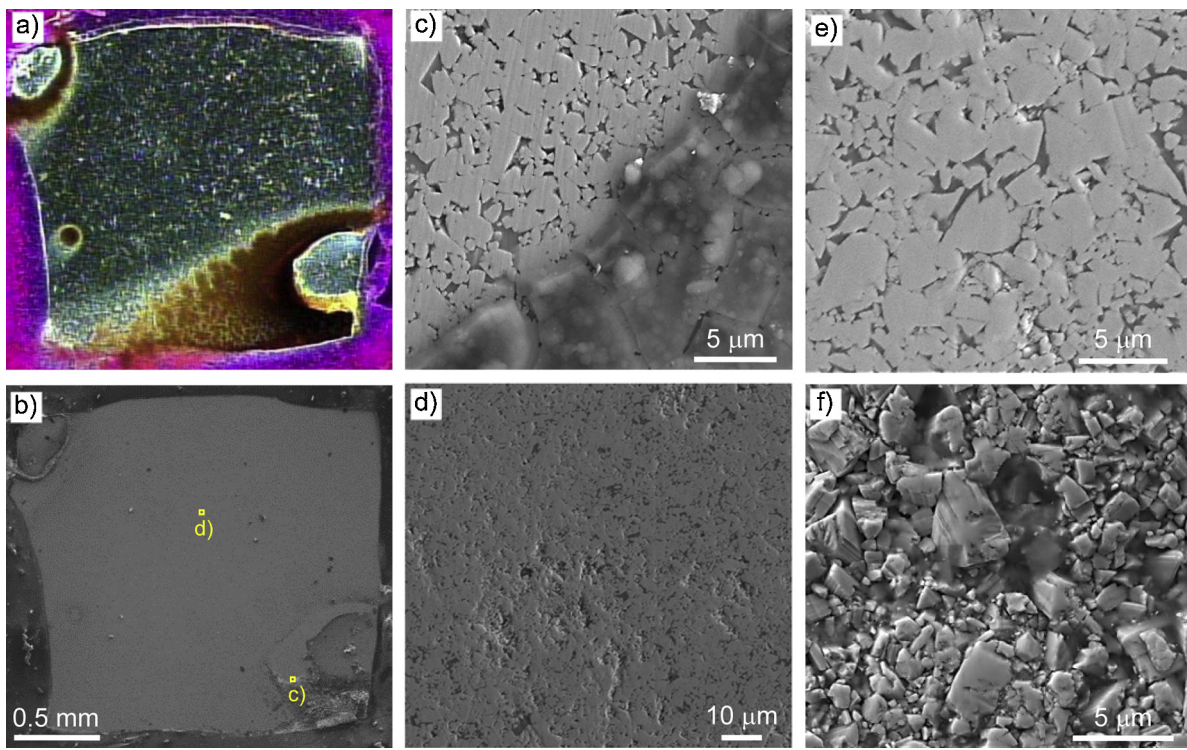


**Fig. 11.** Microscopic characterization of the corrosion of WC-SS-C. (a) Optical image of a sample after 20 h of immersion in 0.05 M NaCl; (b) SEM image of the same surface after the removal of loose corrosion products; (c) a detail of the border of the most attacked area with a small deposit of corrosion products; (d) a central region of the sample; (e) magnification of the central region depicting a region of no attack; (f) magnification of the central region highlighting an attacked area.

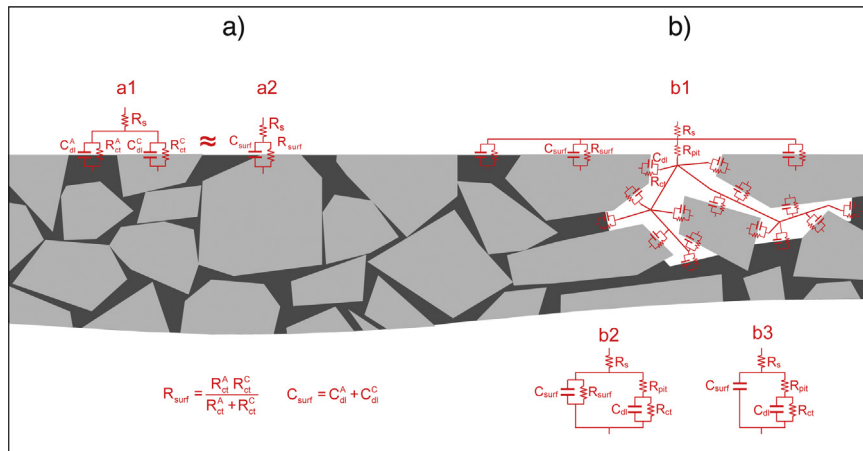


**Fig. 12.** Equivalent electric circuits used to interpret the corrosion of the studied composites. The light grey areas correspond to WC particles and the dark grey colour to the metallic binder matrix.

where  $Y_0$  is the frequency independent admittance of the CPE,  $n$  is the power of the CPE,  $R_{series}$  is the resistance in series and  $R_{parallel}$  the resistance in parallel with the CPE.

The most pertinent parameters are given in Table 3. The values of  $R_{ct}$  for one hour of immersion are in line with those of  $R_p$  obtained by the polarization resistance method.  $R_{ct}$  decreased with time indicating an increase in corrosion rate.

In Section 3.2.2, the entire sample area was considered for the determination of  $R_p$  and the same was done for  $R_{ct}$ . However, the SEM analysis presented in Section 3.3. showed that only the metallic fraction dissolves. The values can be recalculated taking into account only the actual exposed metallic area. This procedure has been done before [6,13,15]. Fig. 13 shows  $R_{ct}$  values recalculated using only the area of the metal phase as given by Table 2. It is

clear that the developed composites have higher  $R_{ct}$  than WC-Co. The values of  $R_{ct}$  for WC-SS and WC-SS-C are now much closer, which is expected since the nature of the corroding phase is the same. Nonetheless, the smaller area of exposed metallic binder in WC-SS makes the metal dissolution to progress in depth faster than in WC-SS-C. This should be the reason for the higher number of small pits scattered along the surface in WC-SS compared to WC-SS-C.

The  $R_{ct}$  gives an underestimation of the corrosion rate because it is related with the activity in the pit and disregards the activity at the surface. However, the discrepancy should not be that significant since the uniform corrosion at the surface is very small compared to the strong attack at the pits, which was confirmed by SEM.

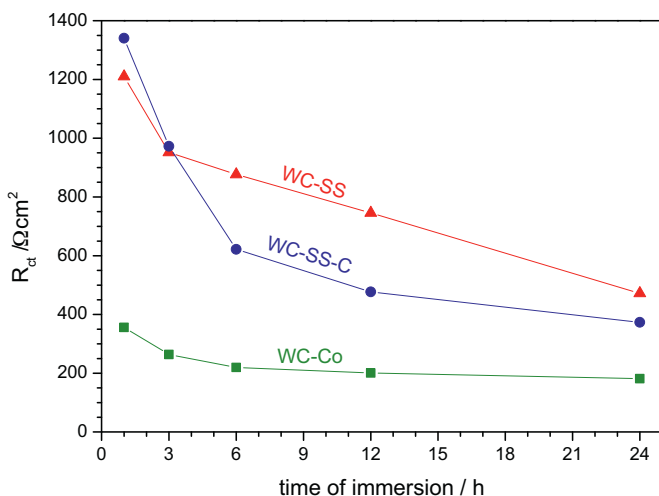


**Fig. 13.** Evolution of  $R_{ct}$  during the first 24 h of immersion, taking into account only the area fraction of the metallic phase.

## 5. Conclusions

Hard-metal composites with WC hard particles and AISI 304L stainless steel as binder phase have been produced with corrosion resistance comparable to the standard WC-Co material. The corrosion of the composites took place by uniform dissolution of the metallic binder phase, together with small pits scattered along the surface (true for stainless steel, not seen with Co) and a few more intense pits associated with dissolution underneath the surface.

## Acknowledgements

This research was sponsored by the Reference Framework (QREN/I&DT/11428/2009) of the European Regional Development Fund (ERDF). It was also financially supported by ERDF through Programa Operacional Factores de Competitividade – COMPETE and national funds through FCT – Fundação para a Ciência e Tecnologia within CICECO project – FCOMP-01-0124-FEDER-037271(FCT Ref. Pest-C/CTM/LA0011/2013).

## References

- [1] G.S. Upadhyaya, *Cemented Tungsten Carbides, Production Properties and Testing*, Noyes Publications, Westwood, NJ, USA, 1998.
- [2] S. Norgen, J. García, A. Blomqvist, L. Yin, Trends in the P/M hard metal industry, *Int. J. Refract. Met. Hard Mater.* 48 (2015) 31–45.
- [3] E.J. Wentel, C. Allen, The erosion-corrosion resistance of tungsten carbide hard metals, *Int. J. Refract. Met. Hard Mater.* 15 (1–3) (1997) 81–87.
- [4] F.J.J. Kellner, H. Hildebrand, S. Virtanen, Effect of WC grain size on the corrosion behavior of WC-Co based硬metals in alkaline solutions, *Int. J. Refract. Met. Hard Mater.* 27 (2009) 806–812.
- [5] M. Pourbaix, *Atlas of electrochemical equilibria*, in: National Association of Corrosion Engineers, 2nd ed., Houston, Texas, USA, 1974, pp. 282–325.
- [6] S. Hochstrasser-Kurz, Y. Mueller, C. Latkoczy, S. Virtanen, P. Schmutz, Analytical characterization of the corrosion mechanisms of WC-Co by electrochemical methods and inductively coupled plasma mass spectroscopy, *Corros. Sci.* 49 (2007) 2002–2020.
- [7] S. Hochstrasser-Kurz, D. Reiss, T. Suter, C. Latkoczy, D. Günther, S. Virtanen, P.J. Uggowitzer, P. Schmutz, ICP-MS, SKPFM, XPS, and microcapillary investigation of the local corrosion mechanisms of WC-Co hardmetal, *J. Electrochem. Soc.* 155 (2008) C415–C426.
- [8] W.A. Badawy, F.M. Al-Kharafi, J.R. Al-Ajmi, Electrochemical behavior of cobalt in aqueous solutions of different pH, *J. Appl. Electrochem.* 30 (2000) 693–704.
- [9] A.J. Hurd, R.L. Kelley, R.G. Eggert, M.-H. Lee, Energy-critical elements for sustainable development, *MRS Bull.* 37 (2012) 405–410.
- [10] S. Chang, S. Chen, Characterization and properties of sintered WC-Co and WC-Ni-Fe hard metal alloys, *J. Alloys Compd.* 585 (2014) 407–413.
- [11] D.S. Konadu, J. van der Merwe, J.H. Potgieter, S. Potgieter-Vermaak, C.N. Machio, The corrosion behaviour of WC-VC-Co hardmetals in acidic media, *Corros. Sci.* 52 (2010) 3118–3125.
- [12] W.J. Tomlinson, N.J. Ayerst, Anodic polarization and corrosion of WC-Co hardmetals containing small amounts of Cr<sub>3</sub>Ca and/or VC, *J. Mater. Sci.* 24 (1989) 2348–2354.
- [13] A.M. Human, H.E. Exner, The relationship between electrochemical behaviour and in-service corrosion of WC based cemented carbides, *Int. J. Refract. Met. Hard Mater.* 15 (1997) 65–71.
- [14] W.J. Tomlinson, C.R. Linzell, Anodic polarization and corrosion of cemented carbides with cobalt and nickel binders, *J. Mater. Sci.* 23 (1988) 914–918.
- [15] A.M. Human, H.E. Exner, Electrochemical behaviour of tungsten-carbide hardmetals, *Mater. Sci. Eng. A* 209 (1996) 180–191.
- [16] G.C. Saha, T.I. Khan, G.A. Zhang, Erosion-corrosion resistance of microcrystalline and near-nanocrystalline WC-17Co high velocity oxy-fuel thermal spray coatings, *Corros. Sci.* 53 (2011) 2106–2114.
- [17] L. Fedrizzi, L. Valentinielli, S. Rossi, S. Segna, Tribocorrosion behaviour of HVOF cermet coatings, *Corros. Sci.* 49 (2007) 2781–2799.
- [18] L. Chen, D. Yi, B. Wang, H. Liu, C. Wu, X. Huang, H. Li, Y. Gao, The selective oxidation behaviour of WC-Co cemented carbides during the early oxidation stage, *Corros. Sci.* 94 (2015) 1–5.
- [19] M. Aristizabal, J.M. Sanchez, N. Rodriguez, F. Ibarreta, R. Martinez, Comparison of the oxidation behaviour of WC-Co and WC-Ni-Co-Cr cemented carbides, *Corros. Sci.* 53 (2011) 2754–2760.
- [20] Q. Zhang, Y. He, W. Wang, N. Lin, C. Wu, N. Li, Corrosion behavior of WC-Co hardmetals in the oil-in-water emulsions containing sulfate reducing *Citrobacter* sp., *Corros. Sci.* 94 (2015) 48–60.
- [21] C.M. Fernandes, L.M. Vilhena, C.M.S. Pinho, F.J. Oliveira, E. Soares, J. Sacramento, A.M.R. Senos, Mechanical characterization of WC-10% AISI 304 cemented carbides, *Mater. Sci. Eng. A* 618 (2014) 629–636.
- [22] C.M. Fernandes, A.M.R. Senos, M.T. Vieira, Control of eta carbide formation in tungsten carbide powders sputter-coated with (Fe/Ni/Cr), *Int. J. Refract. Met. Hard Mater.* 25 (2007) 310–317.
- [23] C.M. Fernandes, A.M.R. Senos, Cemented carbide phase diagrams: a review, *Int. J. Refract. Met. Hard Mater.* 29 (2011) 405–418.
- [24] B.J. Marques, C.M. Fernandes, A.M.R. Senos, Sintering, microstructure and properties of WC-AISI304 powder composites, *J. Alloys Compd.* 562 (2013) 164–170.
- [25] <http://imagej.nih.gov/ij/> (last view on 12.07.15).
- [26] S.I. Cha, K.H. Lee, H.J. Ryu, S.H. Hong, Effect of size and location of spherical pores on transverse rupture strength of WC-Co cemented carbides, *Mater. Sci. Eng. A* 486 (2008) 404–408.
- [27] M.C. Weidman, D.V. Esposito, I.J. Hsu, J.G. Chen, Electrochemical stability of tungsten and tungsten monocarbide (WC) over wide pH and potential ranges, *J. Electrochem. Soc.* 157 (2010) F179–F188.
- [28] M.E. Orazem, B. Tribollet, *Electrochemical Impedance Spectroscopy*, Wiley, 2008, pp. 233.
- [29] G.J. Brug, A.L.G. van den Eeden, M. Sluyters-Rehbach, J.H. Sluyters, The analysis of electrode impedances complicated by the presence of a constant phase element, *J. Electroanal. Chem.* 176 (1984) 275–295.